Analysis and Optimization of Wireless Power and Information Dual Transfer in Multicoil System

Wanying Weng, *Student Member, IEEE*, Jiande Wu, *Senior Member, IEEE*, Long Qin, Hao Chen, Yan Deng, *Senior Member, IEEE*, and Xiangning He, *Fellow, IEEE*

***Abstract*—In magnetically coupled resonant (MCR) wireless power transfer systems, intermediate coils are used to extend power transfer distance. The complex magnetic coupling among multiple coils poses a challenge for simultaneous wireless power and data transfer. Wireless power and information dual transfer (WPIDT) is recently proposed to modulate the transmitting data on one dc side and receives it on the other dc side. In this article, the design and optimization of WPIDT systems with any number of intermediate coils is investigated. First, a general reduced-order model of the multicoil MCR channel is developed. The information transmission properties are analyzed in the model by scattering parameters. Accordingly, the matching circuits for communication are studied to optimize for higher transfer gain. The transfer gain can be simultaneously optimized for both upward and downward communication in a symmetrical coil arrangement. Finally, a 27.7-W five-coil WPIDT prototype system is developed and tested to validate the theoretical analysis. The experiments achieve bidirectional data transfer at 20kbps.**

***Index Terms*—Intermediate coils, reduced order model, simultaneous wireless power and information/data transfer (SWPIT/SWPDT), wireless power and information dual transfer (WPIDT), wireless power transfer (WPT).**

I. Introduction

WIRELESS power transfer (WPT) technology facilitates power transmission without the use of cables, thereby improving the safety, convenience, and mobility [1]. Owing to these advantages, WPT has been extensively studied and applied in diverse fields, including electrical vehicles, biomedical implants, undersea applications, etc. [2]. In these applications, effective communication between the transmitter and receiver is essential for achieving optimal performance, as it enables precise control and system monitoring [3], [4], [5], [6]. This necessity has prompted extensive research into simultaneous wireless power and information/data transfer (SWPIT/SWPDT) [7].

Intermediate coils can be inserted between the transmitter and receiver coils to extend the delivery distance while improving efficiency [8], [9]. This approach has been widely adopted in magnetically coupled resonant wireless power transfer (MCR-WPT) [10]. However, implementing SWPIT in MCR-WPT systems with multiple coils is challenging due to cross-coupling of multiple coils. Cross-coupling complicates the transmission properties of the multicoil MCR channel, making it hard to assess and improve the attenuation in the MCR channel.

In conventional SWPIT methods, both communication and power transmission are achieved through inductive links. SWPIT can be implemented in two distinct ways [3], [4], [7] using separate channels for power and information transfer or using a single channel for both. The former method requires additional coils dedicated to information transmission [11], [12], [13], [14]. For instance, in [11], [12], and [13], data is transmitted via a separate pair of coils, while [14] utilizes the harmonic components of the power waveform to transmit information through an additional coil.

Although adding coils simplifies the design of the information channel, it inevitably increases system complexity and physical volume. In contrast, the latter method multiplexes the power channel to transfer information [15], [16], [17], [18], [19], [20], [21]. In [15] and [16], an extra resonant tank is created by adding coupled inductors, enabling power and data to be transmitted at distinct frequency carriers. In [17], a parallel data transfer circuit is introduced alongside the original power transfer circuit. Wei et al. [18] and Wang et al. [19] exploit the additional coupling mechanism resulting from the physical structure of coils for data transfer. Ahmadi et al. [20] regulates the transmitter's load network to generate data envelope in the power carrier. In [21], different frequency carriers for data are hybridized in the modulation of power waves. Methods that use a single channel for power and information transfer benefit from less coils, but the information channel must be carefully designed to match the power transfer topology.

The separate-channel SWPIT method is unsuitable for multicoil MCR-WPT systems, as incorporating additional coils for information transmission substantially increases cross-talk interference between the power and data links, thereby elevating system complexity and cost. Using the single-channel SWPIT method in multicoil systems remains a significant challenge. It is essential to confirm the feasibility and impact of information transfer within the designed system. Hence, a general design model of MCR-WPT systems with any number of coils is advantageous.

Received 15 April 2025; revised 13 June 2025 and 21 July 2025; accepted 18 August 2025. Date of publication 25 August 2025; date of current version 22 October 2025. This work was supported by the National Natural Science Foundation of China under Grant 52350003. Recommended for publication by Associate Editor K. Ngo. *(Corresponding author: Jiande Wu.)*

The authors are with the College of Electrical Engineering, Zhejiang University, Hangzhou 310027, China. (e-mail: wyweng@zju.edu.cn; eewjd@zju.edu.cn; lqin@zju.edu.cn; eechenhao@zju.edu.cn; dengyan@zju.edu.cn; hxn@zju.edu.cn).

Color versions of one or more figures in this article are available at https://doi.org/10.1109/TPEL.2025.3602062.

Digital Object Identifier 10.1109/TPEL.2025.3602062

In [22] and [23], SWPIT is successfully implemented in a five-coil system using single-channel methods. Yang et al. [22] introduces SWPIT in a domino-resonator system for the first time, utilizing dual-resonance-band coils, while [23] enhances both power and information transfer characteristics through a bipolar coil structure. However, these methods are limited to coils with specialized designs. The injected high-frequency information signals are compensated through uniform configurations applied to each coil. As the number of coils changes, variations in coil output characteristics necessitate adjustments to the electrical components used for compensation. Consequently, the information channel must be redesigned and optimized, leading to increased complexity.

In our previous work [24], a novel method termed wireless power and information dual transfer (WPIDT) is proposed, which modulates the information signal on one dc side and receives it on the other dc side by exploiting the frequency-mixing effect of the inverter and rectifier. WPIDT requires no additional coil design, thus minimizing system configurations while maintaining scalability for integration with any number of intermediate coils. In this article, a general channel model for multicoil systems is developed. This model comprehensively accounts for nonideal parameters and can be universally extended to various coil configurations without restriction. The information transfer characteristics are studied, considering the arrangement and parameters of all the coils. Cross-coupling effects of multiple coils are included. A symmetric feature between downward and upward communication has been demonstrated in detail, confirming the effectiveness of duplex communications in the WPIDT system.

The main contributions of this article are as follows.

1) The power and information transfer characteristics based on scattering parameters are modeled. This article is the first to demonstrate the general feature of MCR channels with multiple intermediate coils using these parameters.
2) A systematic analysis for optimizing the transfer gain of the information is investigated. A rigorous proof is provided, showing that the transfer gain can be simultaneously optimized for duplex communications in a symmetrical coil arrangement.

The rest of this article is organized as follows. Section II overviews the principles of WPIDT technique. Section III provides the system modeling and optimization. Section IV offers a detailed design of the dc sides in the system. Finally, a five-coil WPIDT prototype is constructed to validate the proposed analysis. Finally, Section VI concludes this article.

II. Principle of WPIDT System

A typical MCR-WPT system consists of an inverter on the transmitter for dc-ac conversion, a rectifier on the receiver for ac-dc conversion, and bandpass MCR coils. WPIDT systems integrate communication by adding information sources on the dc sides. The dual communication processes in a WPIDT system are shown in Fig. 1. For clarity, the transmitter is divided into the front side and the dc-ac inverter, while the receiver comprises the ac-dc converter and the load side.

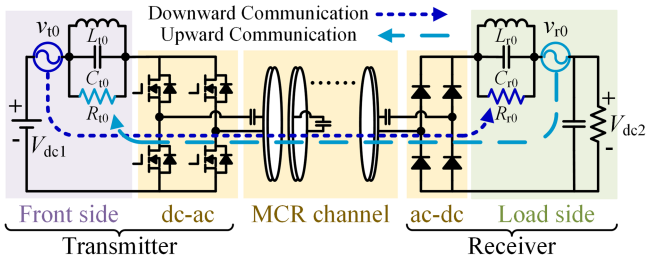

Fig. 1. Duplex communications in the WPIDT system.

In Fig. 1, downward and upward communications are illustrated by dark blue and light blue dashed lines, respectively. To retrieve the information signal, an *RLC* circuit consisting of R_{t0}, C_{t0}, and L_{t0} (R_{r0}, C_{r0}, and L_{r0}) is added to the front (load) side. In downward communication link, the introduced information source $v_{t0}(t)$ and the power source V_{dc1} are in series connected on the front side. The information signal is transmitted through the MCR channel and received at the resistor R_{r0} on the load side. In upward communication link, another information source $v_{r0}(t)$ is introduced on the load side and received at the resistor R_{t0} on the front side.

The key aspect of WPIDT is that the inverter and the rectifier function as a pair of synchronous mixers [24]. These mixers operate at a high frequency f_s (MHz), while $v_{t0}(t)$ or $v_{r0}(t)$ transmits a low-frequency signal in the range of tens of kHz. The mixers allow the low-frequency information signal to be converted to the sideband of the high-frequency power carrier, enabling it to pass through the bandpass MCR channel.

Fig. 2 illustrates the transfer process of WPIDT. In Fig. 2(a), each process of the simultaneous power and information is indicated in the circuit. For information transfer, the matching *RLC* circuits are tuned to the information carrier frequency f_m so they act as a resistor in steady state. The capacitor C_d is considered as a short circuit in frequency f_m. Besides, the *RLC* circuits has few impacts on the dc power. Letting

$$e_{t0}\ (t) = V_{\mathrm{dc1}}\ + v_{t0}\ (t) = V_{\mathrm{dc1}}\ + V_{t0}\cos\left(\omega_m t\right) \tag{1a}$$

$$e_{r0}\ (t) = V_{\mathrm{dc2}}\ + v_{r0}\ (t) = V_{\mathrm{dc2}}\ + V_{r0}\cos\left(\omega_m t - \varphi\right) \tag{1b}$$

where ω_m is the angular frequency of the information carrier, and φ is the phase shift of the information carrier on the load side.

$s_{\mathrm{t}}(t)$ and $s_{\mathrm{r}}(t)$ are unit square waves, described as

$$s_t\ (t) = \begin{cases} 1, \frac{k}{f_s} \le t \le \frac{k+1/2}{f_s} \\ -1, \frac{k+1/2}{f_s} \le t \le \frac{k+1}{f_s} \end{cases} \quad k \in Z \tag{2a}$$

$$s_r\ (t) = s_t\ (t - \theta/\omega_s) \tag{2b}$$

where θ is the phase shift of the power carrier between the transmitter and receiver.

Assuming that the information signal is much smaller than the power signal, the ac sides of the dc–ac/ac–dc converters on the transmitter and receiver can be expressed as

$$e_t\ (t) = e_{t0}\ (t) \cdot s_t\,(t) \tag{3a}$$

$$e_r\ (t) = e_{r0}\ (t) \cdot s_r\,(t)\,. \tag{3b}$$

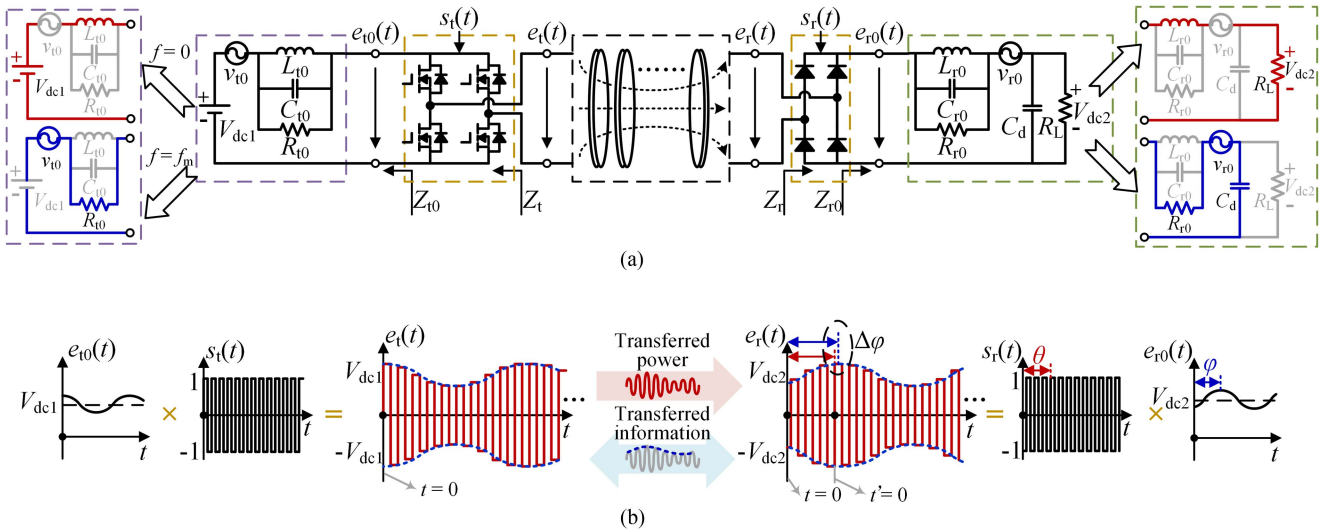

Fig. 2. The transfer process of the WPIDT system. (a) Structure of the system. (b) Waveforms of simultaneous power and information.

The waveforms of $e_{t0}(t)$, $s_t(t)$, $e_{r0}(t)$, and $s_r(t)$ are sketched in Fig. 2(b). Here, θ is determined by the channel characteristics at the power transfer frequency f_s, and φ is determined by the channel characteristics at the information transfer frequency.

Considering that the Fourier series of $s_t(t)$ is

$$s_t\ (t) = \sum_{k\in Z} \frac{4}{(2k+1)\,\pi} \sin\left[(2k+1)\,\omega_s t\right] \tag{4}$$

and focusing on fundamental components of the square wave $s_t(t)$, the significant components of $e_t(t)$ can be derived as

$$e_t\ (t) = \frac{4V_{\rm dc1}}{\pi} \sin\left(\omega_s t\right) + \frac{2V_{t0}}{\pi} \sin\left(\left(\omega_s+\omega_m\right) t\right) + \frac{2V_{t0}}{\pi} \sin\left(\left(\omega_s-\omega_m\right) t\right). \tag{5}$$

Considering the phase shift on the load side, we define $t' = t\text{-}\theta/\omega_s$. Due to the slight difference in the center frequencies of power and information within the MCR channel, let $\Delta\varphi = \theta\text{–}\varphi$. The Fourier series of $s_{\rm r}(t')$ is the same as (4). Thus, $e_{\rm r}(t')$ can be derived as

$$e_r\ (t') = \frac{4V_{\rm dc2}}{\pi} \sin\left(\omega_s t'\right) + \frac{2V_{r0}}{\pi} \sin\left(\left(\omega_s+\omega_m\right) t' - \Delta\varphi\right) + \frac{2V_{r0}}{\pi} \sin\left(\left(\omega_s-\omega_m\right) t' - \Delta\varphi\right). \tag{6}$$

When $f_s >> f_m$, $\Delta\varphi$ results from the difference in the center frequencies is small when compared to the low-frequency carrier $f_{\rm m}$. The effect of $\Delta\varphi$ on $v_{r0}(t)$ can be neglected.

To simplify the analysis, the power transfer process and the communication process are modeled separately. Disregarding the communication components, the power transfer process is modeled in Fig. 3(a), where $V_{\rm dc1}$ and $V_{\rm dc2}$ in (5) and (6) are represented as an equivalent voltage source and resistor. Similarly, since v_{t0} and v_{r0} are small ripples attached to the power signals, the communication process can be modeled in Fig. 3(b). Here, v_{t0} or v_{r0}, along with the *RLC* circuit, is represented by v_t or v_r

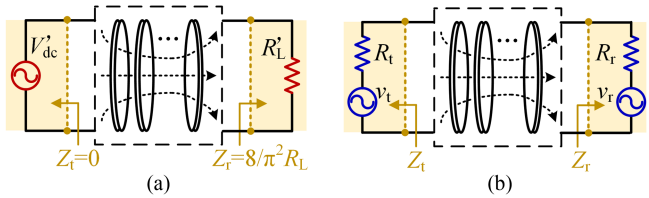

Fig. 3. Equivalent circuit model of the WPIDT system. (a) Power transfer process. (b) Information transfer process.

with R_t or R_r [24]. The equivalent impedances $R_t = 8/\pi^2 \cdot R_{t0}$, and $R_r = 8/\pi^2 \cdot R_{r0}$.

As shown in Fig. 3, downward communication resembles envelope modulation, where $V_{\rm dc2}$ and v_{r0} are regards as the outputs of the transferred $V_{\rm dc1}$ and v_{t0}. Similarly, upward communication resembles backscatter communication. The transfer relation of these sources require analysis through cross-coupling in the multicoil channel.

III. Channel Modeling and Optimization

The WPIDT system transfers power at the frequency f_s and carries information at the frequency $f_s \pm f_m$, enabling the simultaneous transmission of power and information within a shared frequency band. To assess the feasibility of information transfer in a general multicoil channel, it is critical to quantify the attenuation in the shared frequency band.

A. Model and Features of N-coil MCR-WPT System

The schematic of the N-coil MCR channel is illustrated in Fig. 4. The relevant variables are defined as follows:

L_p, R_p, and C_p ($p = 12, \ldots, N$) represent the self-inductance, equivalent series resistance and compensation capacitance of the pth coil, respectively.

K_{pq} denotes the coupling coefficient between pth coil and qth coil, where $K_{pq} = K_{qp}$. and $p, q \in [1, 2, \ldots, N]$.

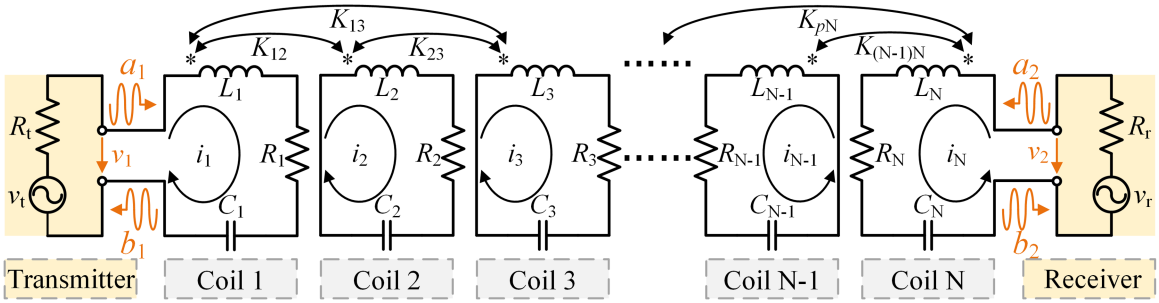

Fig. 4. Schematic of the MCR channel with N coils.

ω_s is the operating angular frequency. All coils are tuned at the same angular frequency ω_s in practice.

According to Kirchhoff's Voltage Law, a high-order matrix equation is derived to model the MCR channel as follows:

$$\begin{bmatrix} V_t \\ 0 \\ \vdots \\ V_r \end{bmatrix} = \begin{bmatrix} Z_1 + R_t & jK_{12} & \cdots & jK_{1N} \\ jK_{21} & Z_2 & \cdots & jK_{2N} \\ \vdots & \vdots & \ddots & \vdots \\ jK_{N1} & jK_{N2} & \cdots & Z_N + R_r \end{bmatrix} \begin{bmatrix} I_1 \\ I_2 \\ \vdots \\ I_N \end{bmatrix}. \quad (7)$$

where $Z_p = j\omega_s L_p + 1/(j\omega_s C_p) + R_p$. Two matching resistors, R_r and R_t, are placed on the first and Nth coils, respectively.

These equations can be simplified by separating the equations for the end coils from those for the intermediate coils [25].

The current in intermediate coils ($p = 2, \ldots, N\text{-}1$) is redefined as a vector $\boldsymbol{I} = [I_2 \quad \cdots \quad I_{(N-1)}]^T$. Hence,

$$0 = \begin{bmatrix} \boldsymbol{\alpha} & \boldsymbol{M} & \boldsymbol{\beta} \end{bmatrix} \begin{bmatrix} I_1 \\ \boldsymbol{I} \\ I_N \end{bmatrix} \quad (8)$$

where

$$\boldsymbol{\alpha} = \begin{bmatrix} jK_{21} \\ jK_{31} \\ \vdots \\ jK_{(N-1)1} \end{bmatrix},$$

$$\boldsymbol{M} = \begin{bmatrix} Z_2 & jK_{23} & \cdots & jK_{2(N-1)} \\ jK_{32} & Z_3 & \cdots & jK_{3(N-1)} \\ \vdots & \vdots & \ddots & \vdots \\ jK_{(N-1)2} & jK_{(N-1)3} & \cdots & Z_{(N-1)} \end{bmatrix},$$

$$\boldsymbol{\beta} = \begin{bmatrix} jK_{2N} \\ jK_{3N} \\ \vdots \\ jK_{(N-1)N} \end{bmatrix}. \quad (9)$$

By solving (8), the transform relation is derived as

$$\boldsymbol{I} = -\boldsymbol{M}^{-1}(\boldsymbol{\alpha} I_1 + \boldsymbol{\beta} I_N). \quad (10)$$

Substituting (10) into (7) gives

$$\begin{cases} V_t = \left[\boldsymbol{\alpha}^T \boldsymbol{G} \boldsymbol{\alpha} + Z_1 + R_t\right] I_1 + \left[\boldsymbol{\alpha}^T \boldsymbol{G} \boldsymbol{\beta} + jK_{1N}\right] I_N \\ V_r = \left[jK_{N1} + \boldsymbol{\beta}^T \boldsymbol{G} \boldsymbol{\alpha}\right] I_1 + \left[\boldsymbol{\beta}^{\mathrm{T}} \boldsymbol{G} \boldsymbol{\beta} + Z_N + R_{\mathrm{r}}\right] I_N \end{cases} \quad (11)$$

where for simplicity, it is defined

$$\boldsymbol{G} = -\boldsymbol{M}^{-1}. \quad (12)$$

Although the precise effect of the intermediate coils on the end coils is complicated, (11) shows that the synthetic reflection can be approximated as a coupling coefficient with a decay factor. The N-coil model in (7) can be described by the reduced-order model in (11).

To investigate the general features of the synthetic reflection in intermediate coils, scattering parameters (*S*-parameters) are used because they are easy to quantify the transfer properties of information signals and friendly for measurement [26]. In Fig. 4, v_1 and v_2 represent the input and output port voltages. The incident and reflected waves at the input port are denoted as a_1 and b_1, while the incident and reflected waves at the output port are denoted as a_2 and b_2, respectively.

Given that $\boldsymbol{M} = \boldsymbol{M}^{\mathrm{T}}$, it follows that $(\boldsymbol{M}^{-1})^{\mathrm{T}} = (\boldsymbol{M}^{\mathrm{T}})^{-1} = \boldsymbol{M}^{-1}$, indicating that $\boldsymbol{G}$ is always symmetric. Subsequently,

$$\boldsymbol{\alpha}^T \boldsymbol{G} \boldsymbol{\beta} = \left(\boldsymbol{\alpha}^T \boldsymbol{G} \boldsymbol{\beta}\right)^T = \boldsymbol{\beta}^T \boldsymbol{G} \boldsymbol{\alpha}. \quad (13)$$

From (13), it is derived that

$$\kappa = \boldsymbol{\alpha}^T \boldsymbol{G} \boldsymbol{\beta} + j K_{1N} = \boldsymbol{\beta}^T \boldsymbol{G} \boldsymbol{\alpha} + jK_{N1}. \quad (14)$$

Here, κ is an inherent parameter associated with the N-coil MCR channel and is unaffected by the applied excitation or the matching resistors.

Based on the definition in [26], S_{21} and S_{12} are deduced as

$$\begin{cases} S_{21} = \frac{2V_2}{V_t} \sqrt{\frac{R_t}{R_r}} = \frac{2\kappa\sqrt{R_r R_t}}{\zeta_t \zeta_r - \kappa^2} \\ S_{12} = \frac{2V_1}{V_r} \sqrt{\frac{R_r}{R_t}} = \frac{2\kappa\sqrt{R_t R_r}}{\zeta_t \zeta_r - \kappa^2} \end{cases} \quad (15)$$

where for simplicity

$$\begin{cases} \zeta_t = \boldsymbol{\alpha}^T \boldsymbol{G} \boldsymbol{\alpha} + Z_1 + R_t \\ \zeta_r = \boldsymbol{\beta}^T \boldsymbol{G} \boldsymbol{\beta} + Z_N + R_r \end{cases}. \quad (16)$$

According to (15), S_{21} is always consistent with S_{12} regardless of κ, ζ_t, and ζ_r. Nonadjacent coupling is completely considered in these expressions. (15) remains satisfied when the arrangement of arbitrary coils is not equidistant.

Furthermore, S_{11} and S_{22} are derived as

$$\begin{cases} S_{11} = 1 - \frac{2R_t \zeta_r}{\zeta_t \zeta_r - \kappa^2} \\ S_{22} = 1 - \frac{2R_r \zeta_t}{\zeta_t \zeta_r - \kappa^2} \end{cases}. \quad (17)$$

Since $\zeta_t \neq \zeta_r$, S_{11}, and S_{22} are not consistent with each other. To facilitate further analysis, two assumptions are made as follows.

1) The intermediate coils are standardized and share the same electrical parameters. Thus, $R_p = R$ for $p = 2, \ldots, N\text{-}1$. Additionally, for simplicity, the first and Nth coils are assumed to be identical, such that $R_1 = R_N$.
2) The arrangement of N coils exhibits central symmetry, i.e., $K_{p1} = K_{(N+1-p)N}$.

Using g_{pq} to denote the entry in row p, column q of the matrix $\boldsymbol{G}$ in (12). $\boldsymbol{G}$ can be rewritten as

$$\boldsymbol{G} = (g_{pq})_{p=2,q=2}^{\mathrm{N}-1,\mathrm{N}-1}, \tag{18}$$

where $g_{pq} = g_{(N+1-p)(N+1-q)}$.

Thus, we have

$$\begin{cases} \boldsymbol{\alpha}^{\mathrm{T}}\boldsymbol{G}\boldsymbol{\alpha} = -\sum_{q=2}^{N-1}\sum_{p=2}^{N-1} g_{pq}K_{p1}K_{q1} \\ \boldsymbol{\beta}^{\mathrm{T}}\boldsymbol{G}\boldsymbol{\beta} = -\sum_{q=2}^{\mathrm{N}-1}\sum_{p=2}^{\mathrm{N}-1} g_{pq}K_{pN}K_{qN} \end{cases}. \tag{19}$$

By letting $p' = N\text{+}1\text{-}p$ and $q' = N\text{+}1\text{-}q$, we obtain

$$\boldsymbol{\beta}^T\boldsymbol{G}\boldsymbol{\beta} = -\sum_{q'=2}^{N-1}\sum_{p'=2}^{N-1} g_{p'q'}K_{p'1}K_{q'1}. \tag{20}$$

Subsequently, it can be derived that

$$\boldsymbol{\alpha}^T\boldsymbol{G}\boldsymbol{\alpha} = \boldsymbol{\beta}^T\boldsymbol{G}\boldsymbol{\beta}. \tag{21}$$

As indicated by (17) and (21), S_{11} and S_{22} can be adjusted by modifying R_t and R_r. Let $R_t = R_r = R_m$, we have $\zeta_t = \zeta_r = \zeta$. By substituting ζ into (17), we obtain $S_{11} = S_{22} = 1\text{-}2R_m\zeta/(\zeta^2\text{-}\kappa^2)$.

Consequently, the transfer properties of the input and output in the N-coil MCR channel can be investigated. A general symmetry in the dual communication links can be established by R_t and R_r. When the assumptions 1) and 2) are satisfied, the reflection (S_{11} and S_{22}) and transmission (S_{21} and S_{12}) coefficients are symmetrical. Thus, similar transfer properties in both downward and upward communication can be achieved.

B. Assessment and Optimization of Communication

In the WPIDT system, optimizing the transfer gain of the information carrier is typically necessary to improve the signal-to-noise ratio (SNR), i.e., S_{21} should be maximized at the carrier frequency.

Based on S-parameters derived in the previous section, this section clarifies the complex relationship among the coupling coefficient K_{pq}, the matching resistor R_m, and S_{21}. This relationship helps to assess and optimize communication. A five-coil MCR channel is built and analyzed through numerical calculations, with the parameters given in Table I.

In the example system, it is assumed that $K_{12} = K_{45}$ is constant, while $K_{23} = K_{34}$ is variable. Let the ratio of K_{23} to K_{12} be denoted as ρ, where

$$\rho = \frac{K_{23}}{K_{12}}. \tag{22}$$

Fig. 5 depicts $|S_{21}|$ for the five-coil MCR channel. In complex coil systems, frequency splitting often occurs readily. The amplitude versus frequency relationship is depicted by purple lines in Fig. 5, with ρ being 0.5, 1, and 1.5, respectively. As ρ decreases, the frequency splitting phenomenon becomes less distinct, but the high-amplitude region narrows.

TABLE I
PARAMETERS OF MULTICOIL WPIDT SYSTEM

Block	Symbol	Quantity	Value/type
Transmitter	Q_{11}, Q_{12}	Switches	GS61008T, 480kHz
	L_{pt}	Inductance	15 uH
	C_{pt}	Capacitance	510 nF
	L_{t0}, C_{t0}, R_{t0}	Matching circuit	15 uH, 0.47 uF, 18.5 Ω
MCR channel	Q_3-Q_4	Switches	GS61008T, 1 MHz
	L_1, C_1, R_1 /L_5, C_5, R_5	First and last coils	4 uH, 6.3 nF, 0.31 Ω
	L_N, C_N, R_N	Intermediate coils	10.2 uH, 2.5 nF, 0.47 Ω
	D_1-D_4	Diodes	SL20100DS
Receiver	L_{r0}, C_{r0}, R_{r0}	Matching circuit	15 uH, 0.47 uF, 18.5 Ω
	Q_{21}, Q_{22}	Switches	GS61008T, 480 kHz
	L_{pr}	Inductance	15 uH
	C_d, C_{pr}	Capacitance	20 uF, 510 nF
	R_L	Load	7.5 Ω

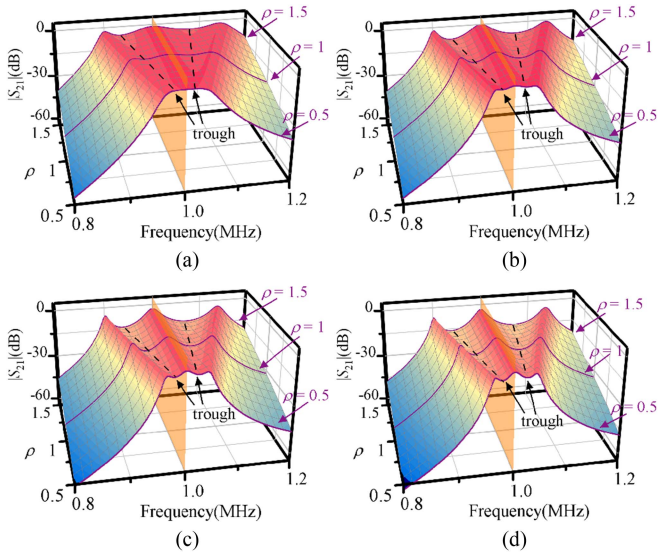

Fig. 5. $|S_{21}|$ versus ρ and the frequency. (a) R_m=12.5 Ω. (b) R_m=25 Ω. (c) R_m=37.5 Ω. (d) R_m=50 Ω.

To evaluate the bandwidth of the channel, a normalized transmission gain G_{T} is introduced. Define $|S_{21}|$ at frequency f_s as the reference gain $\xi_s(\rho)$, and G_T is given by

$$G_T\ (f, \rho) = 20\log_{10}\frac{|S_{21}|}{\xi_s\ (\rho)}. \tag{23}$$

Fig. 6 shows G_T corresponding to Fig. 5. The 6 dB bandwidth of the MCR channel is defined as the frequency range where $G_T \geq -6$ dB, as indicated by dashed lines. The effective region, which is defined as the red region enclosed by dashed lines, represents the frequency range where the information signal can be efficiently transferred.

It can be observed that when ρ is large, the effect of the trough region is rather significant. When ρ is small, the bandwidth is relatively narrow. For optimal performance, ρ should be around

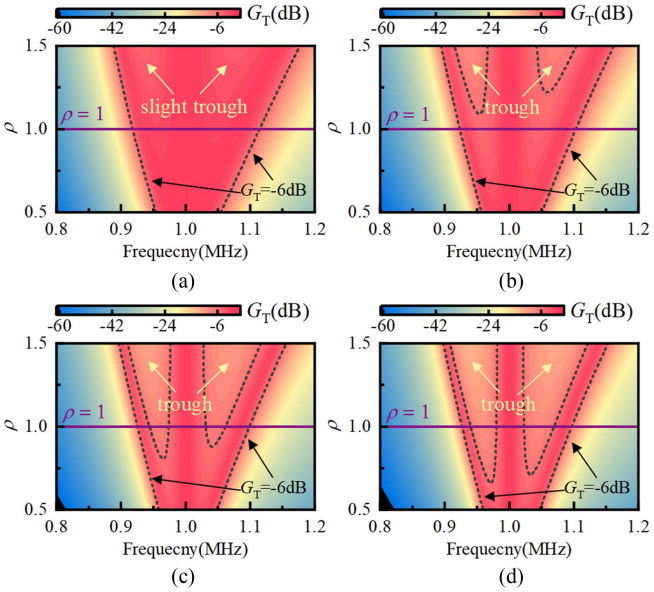

Fig. 6. G_T versus ρ and the frequency. (a) $R_m = 12.5\ \Omega$. (b) $R_m = 25\ \Omega$. (c) $R_m = 37.5\ \Omega$. (d) $R_m = 50\ \Omega$.

1. Moreover, the change in R_m from Fig. 6(a)–(d) affects the effective region. In Fig. 6(c) and (d), the area around the trough is no longer included in the efficient region where $\rho = 1$. Hence, a suitable R_m is beneficial to the communication.

The optimal R_m in a maximized S_{21} can be determined by solving $\partial|S_{21}|/\partial R_m = 0$, where $S_{21} = 2\kappa R_m/(\zeta^2\text{-}\kappa^2)$. The matrices in κ and ζ need to be analyzed.

First, express M in terms of its real and imaginary parts

$$\boldsymbol{M} = \boldsymbol{M}_1 + \mathrm{j}\boldsymbol{M}_2 \tag{24}$$

where both $\boldsymbol{M}_1$ and $\boldsymbol{M}_2$ are real matrices.

Next, it can be derived

$$\boldsymbol{M}^{-1} = \left(\boldsymbol{M}_2^{-1} - \mathrm{j}\boldsymbol{M}_1^{-1}\right)\left(\boldsymbol{M}_1\boldsymbol{M}_2^{-1} + \boldsymbol{M}_2\boldsymbol{M}_1^{-1}\right)^{-1}. \tag{25}$$

Referring to (12)

$$\boldsymbol{G} = -\left(\boldsymbol{M}_2^{-1} - \mathrm{j}\boldsymbol{M}_1^{-1}\right)\left(\boldsymbol{M}_1\boldsymbol{M}_2^{-1} + \boldsymbol{M}_2\boldsymbol{M}_1^{-1}\right)^{-1}. \tag{26}$$

Considering the similar parameters in the expression for $\boldsymbol{M}_1$ and $\boldsymbol{M}_2$, $\boldsymbol{G}$ can be further simplified as

$$\boldsymbol{G} = (-1 + \mathrm{j}\boldsymbol{M}_2/R)\left(R + \boldsymbol{M}_2^2/R\right). \tag{27}$$

Subsequently, κ and ζ in S_{21} can be expressed as

$$|S_{21}| = \frac{2R_m\sqrt{k_1^2 + k_2^2}}{\sqrt{\left(z_1^2 - z_2^2 - k_1^2 + k_2^2\right)^2 + 4(z_1z_2 - k_1k_2)^2}} \tag{28}$$

where

$$\begin{aligned} z_1 &= -\boldsymbol{\alpha}^T\left(R + \boldsymbol{M}_2^2/R\right)\alpha + R_1 + R_\mathrm{m} \\ z_2 &= \boldsymbol{\alpha}^T\left(\boldsymbol{M}_2/R\right)\left(R + \boldsymbol{M}_2^2/R\right)\alpha + \omega_s L_1 - 1/\omega_s C_1 \\ k_1 &= -\boldsymbol{\alpha}^T\left(R + \boldsymbol{M}_2^2/R\right)\beta \\ k_2 &= \boldsymbol{\alpha}^T\left(\boldsymbol{M}_2/R\right)\left(R + \boldsymbol{M}_2^2/R\right)\beta + K_{1N}. \end{aligned} \tag{29}$$

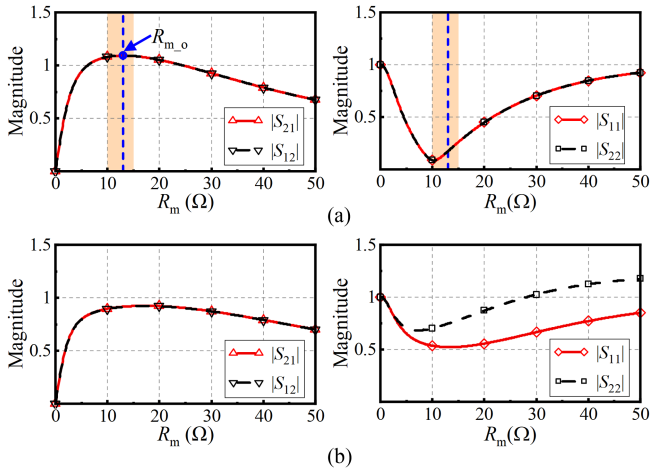

Fig. 7. Transfer properties under. (a) Symmetrical arrangement. (b) Asymmetrical arrangement.

TABLE II
SYMMETRICAL AND ASYMMETRICAL COIL ARRANGEMENT

Arrangement	Symbol	Parameter	Value/type
Symmetrical	d_{12}, d_{23}, d_{34}, d_{45}	Distance	55 mm, 90 mm, 90 mm, 55 mm
Asymmetrical	d_{12}, d_{23}, d_{34}, d_{45}	Distance	60 mm, 85 mm, 110 mm, 50 mm

Substituting (28) into the differential equation yields

$$\begin{aligned} &\left(z_1^2 - z_2^2 - k_1^2 + k_2^2\right)^2 + 4(z_1z_2 - k_1k_2)^2 \\ &- 2R_\mathrm{m}\left[\left(z_1^2 - z_2^2 - k_1^2 + k_2^2\right)z_1 + 2\left(z_1z_2 - k_1k_2\right)z_2\right] = 0. \end{aligned} \tag{30}$$

The optimal R_m deduced from (30) is denoted as R_{m_o}. Take a two-coil system as an example. It can be derived that α, β, and $\boldsymbol{M}$ are zero. In this case, $z_1 = R_1 + R_m$, $z_2 \approx 0$, $k_1 = 0$, and $k_2 = K_{1N}$. As a result, R_{m_o} is resolved as $R_{m\_o} = \sqrt{R_1^2 + K_{12}^2}$.

In the case of the five-coil system, a numerical solution was implemented in MATLAB, and the results are shown in Fig. 7. As given in Table II, both symmetrical and asymmetrical arrangements are considered. In the symmetrical arrangement, d_{12} and d_{23} yield a ρ value of approximately 1, with a deviation that is less than 10%. The asymmetrical arrangement is derived from modifications to the symmetrical arrangement.

In Fig. 7(a), the results under the symmetrical arrangement are presented. In Fig. 7(a1), $|S_{21}|$ and $|S_{12}|$ coincide with $R_{m\_o} = 13\ \Omega$. In Fig. 7(a2), $|S_{11}|$ and $|S_{22}|$ are similar. The minimum $|S_{11}|$ does not align with the maximum $|S_{21}|$ since, in practice, the MCR channel is not lossless.

For comparison, the asymmetrical results are shown in Fig. 7(b). It is observed that although $|S_{21}| = |S_{12}|$, $|S_{11}|$ and $|S_{22}|$ are not similar. The value of $|S_{22}|$ remains large when $|S_{11}|$ is relatively small. The one-sided communication can be optimized in the asymmetrical arrangement, but it is difficult to achieve the same for the other side. In contrast, the symmetrical coil arrangement facilitates better duplex communication and simplifies the optimization process.

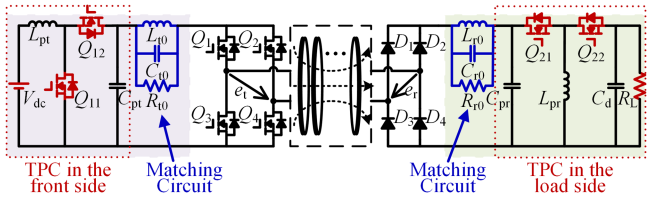

Fig. 8. Circuit schematic of the overall WPIDT system.

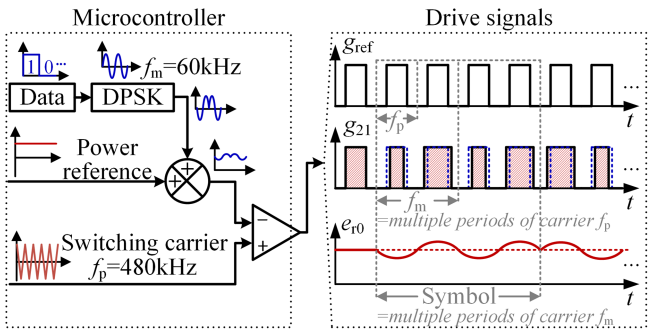

Fig. 9. Control scheme and drive signals of TPCs.

IV. Design of Front and Load Sides

In this section, the design of the front and load sides where the information sources and the matching *RLC* circuits are inserted, is discussed. Talkative power converters (TPCs) [27] are cascaded in the front and load sides to generate dc power embedded with information in a form of small ripples. The schematic of the overall WPIDT system is shown in Fig. 8.

A. Modulation in Front and Load Sides

In Fig. 8, the boost at the front side and the buck-boost at the load side operate as TPCs. Taking the load-side converter as an example, the control scheme of TPCs and the resulted waveforms of drive signals are depicted in Fig. 9. In the microcontroller, data is modulated onto the low-frequency carrier f_m by differential phase shift keying (DPSK) in this article. The waveforms of the drive signals are modulated at the same time. When only the power reference is considered, the PWM sequence for power regulation is denoted as $g_{\rm ref}$. The data modulation on the power reference periodically adds a small duty-cycle perturbation to $g_{\rm ref}$, denoted as g_{21}. This duty-cycle perturbation is akin to sinusoidal pulsewidth modulation, making its base harmonic f_m function as the information signal carrier. The output of the TPC, shown as $e_{\rm r0}$, includes small information ripples superimposed on the dc power voltage. Thus, the TPC can be simplified as a dc power source in series with an information source, as shown in Fig. 2. Among various modulation schemes, DPSK is selected for its robustness under varying load conditions, outperforming amplitude shift keying (ASK) and frequency shift keying (FSK). ASK is sensitive to changes in SNR, while FSK requires a broader bandwidth.

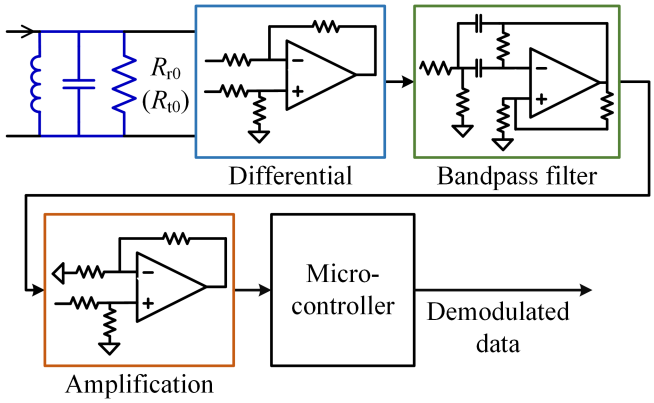

Fig. 10. Demodulation circuit.

B. Demodulation and Adjusting Matching Circuits

The demodulation circuit is connected to the matching circuit, as depicted in Fig. 10. First, a differential circuit is used to sample the signal. Next, a bandpass filter and an amplification circuit is used to condition the signal. The output signal is then processed by a microcontroller for demodulation.

The matching circuits are employed in the communication links to optimize transfer properties while minimizing cross-interference between power transfer and communication. The resistors in matching circuits are not inherent parameters of MCR coils such as the Q-factor, so they can be easily adjusted to optimize the channel bandwidth. With increased bandwidth, the carrier frequency of information signals can be raised, which expands the upper limit of the data rate. In addition to the optimal matching resistors R_{t0} and R_{r0}, careful consideration must be given to the parallel capacitors and inductors to enhance performance. L_{t0} and C_{t0}, as well as L_{r0} and C_{r0}, resonate at the information carrier frequency, expressed as

$$\frac{1}{2\pi\sqrt{L_{t0}C_{t0}}} = \frac{1}{2\pi\sqrt{L_{r0}C_{r0}}} = f_m. \tag{31}$$

The quality factor Q_m of the matching circuit is

$$Q_{\rm mt} = \frac{2\pi f_s L_{t0}}{R_{t0}}$$
$$Q_{\rm mr} = \frac{2\pi f_s L_{r0}}{R_{r0}}. \tag{32}$$

A higher quality factor improves the frequency-selective characteristic of the matching circuit. However, the large quality factor also narrows the signal bandwidth, which limits the baud rate of the data transmission [18]. Therefore, the quality factor must be carefully selected to balance filtering performance and data rate. The inductor and capacitor values are determined according to the desired quality factor. Typically, the quality factor is chosen to be less than 10.

V. Experiments and Validation

A five-coil experimental prototype was built to validate the theoretical analysis, as shown in Fig. 11, with parameters listed in Tables I and II. The circuit configuration is identical to that

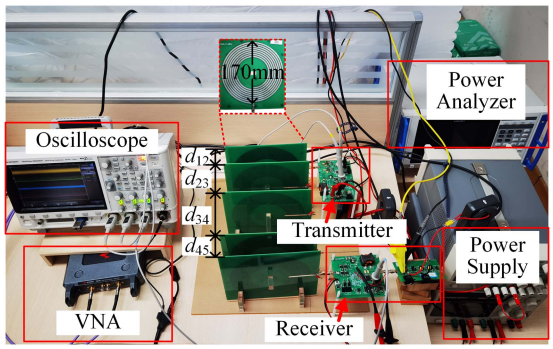

Fig. 11. Experimental prototype.

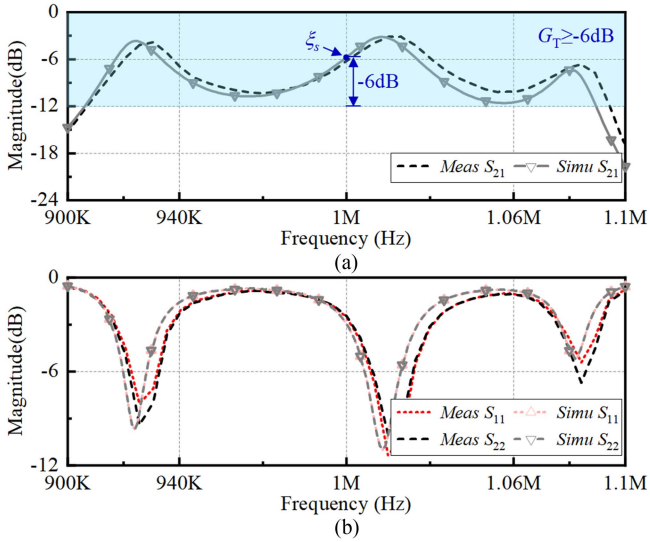

Fig. 12. Measured and simulated S-parameters of the five-coil prototype with symmetric coil arrangement as in Table II. (a) S_{21}. (b) S_{11} and S_{22}.

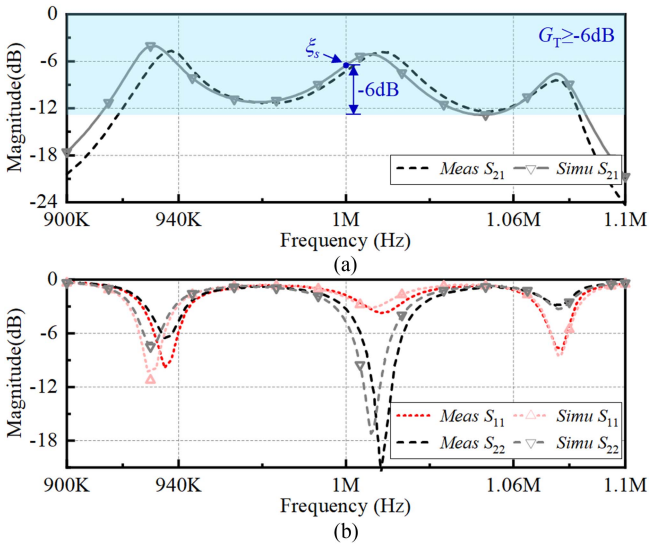

Fig. 13. Measured and simulated S-parameters of the five-coil prototype with asymmetric coil arrangement as in Table II. (a) S_{21}. (b) S_{11} and S_{22}.

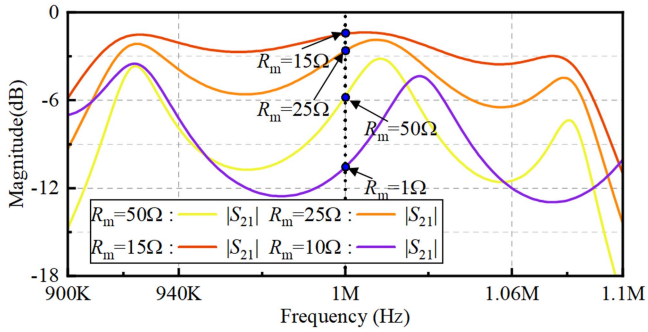

Fig. 14. Optimization of R_{m_o}.

in Fig. 8. Fabricating effective Litz wires in MHz systems is difficult due to the need of extremely small strand diameters. In the prototype, the coils are made using printed circuit board technology, offering advantages in consistency and compactness. Experiments were conducted as follows.

First, to verify the theoretical multicoil model, S-parameters for symmetrical and asymmetrical coil arrangements were simulated and measured, as shown in Figs. 12 and 13. R_m in the VNA (KEYSTGHT P9370B) is set at 50 Ω. Since S_{12} equals S_{21}, only S_{21} is displayed. In Figs. 12(a) and 13(a), the measured S_{21} is in black solid lines. The simulated S_{21} is calculated by MATLAB according to (15). The coupling coefficients in matrices α, β, and $\boldsymbol{M}$ are measured by a handheld LCR meter according to the coil arrangements in Table II. It is evident that the simulated results align well with the measured results.

S_{11} and S_{22} are, respectively, displayed in Figs. 12(b) and 13(b). The simulated S_{11} and S_{22} are calculated by (17). Apparently, the simulated results also align well with the measured results. According to (21), S_{11} and S_{22} only coincide with each other when the coil arrangement is symmetrical. Therefore, S_{11} is well aligned with S_{22} in Fig. 12(b), while S_{11} does not align with S_{22} in Fig. 13(b).

The 6 dB band according to (23) is shown in Figs. 12(a) and 13(a). In the symmetrical WPIDT system [see Fig. 12(a)], the 6 dB band spans approximately 920 kHz to 1.08 MHz.

Next, R_m is optimized in the symmetrical prototype. The curve of $|S_{21}|$ versus R_m is shown in Fig. 14. The maximum $|S_{21}|$ is obtained near $R_{m\_o} = 13\,\Omega$ according to (30). Referring to Fig. 7(a1), the magnitude of $|S_{21}|$ exhibits little variation near $R_{m\_o} = 13\,\Omega$. Thus, $R_m = 15\,\Omega$ is selected as the optimal resistor. In Fig. 14, it is seen that $|S_{21}|$ is larger when $R_m = 15\,\Omega$ in comparison of $R_m = 50\,\Omega$. Considering the frequency mixing effect in the experimental prototype (see Fig. 3), $R_{t0} = R_{r0} = 18.5\,\Omega$.

Owning to the analysis and optimization, duplex communications are achievable in the WPIDT system within the 6 dB bandwidth. The information carrier frequency is set at $f_m = 60$ kHz so the mixed frequencies are 1.06 MHz and 940 kHz, respectively, which is within the 6 dB bandwidth. The data rate is 20 kbps.

The dc side waveforms (measured by KEYSIGHT DSOX3024T) of the WPIDT system are shown in Fig. 15.

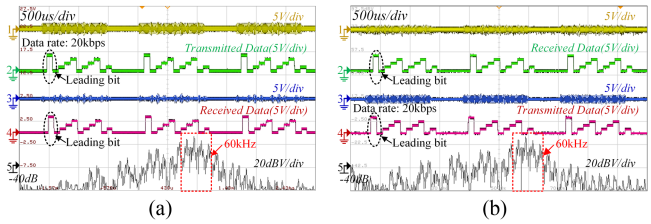

Fig. 15. Waveforms on the DC sides. (a) Downward communication. (b) Upward communication.

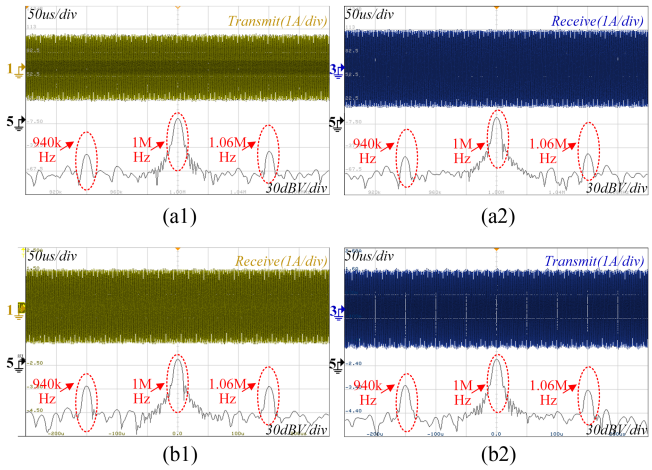

Fig. 16. Waveforms on the ac sides. (a1) Current on the transmitter in downward transmission. (a2) Current on the receiver in downward transmission. (b1) Current on the transmitter in upward transmission. (b2) Current on the receiver in upward transmission.

Fig. 15(a) shows the waveforms in downward communication. The transmitted data (CH2) are modulated on the voltage v_{t0} (CH1). The received data (CH4) are demodulated from the voltage v_{r0} (CH3). The data sequence is "0123012301," where the first bit is the leading bit. Fig. 15(b) shows the waveforms in upward communication, which are similar to those in downward communication. The fast Fourier transform (FFT) of the transmitted voltages is presented in CH5, where the carrier frequency ($f_m = 60$ kHz) of the data is prominently displayed.

The ac side waveforms of the WPIDT system are shown in Fig. 16. Fig. 16(a) shows the ac currents on the transmitter (a1) and on the receiver (a2) in downward communication. As can be observed, the information ripple integrated on the dc sides generates a data envelope on the power carrier, which exists at both the transmitter and receiver of the duplex communication. This envelope is shown in Fig. 17. The FFT spectrum of the ac waveforms clearly shows the resonant frequency component ($f_s = 1$ MHz) and the mixed components ($f = 1$ MHz±60 kHz), confirming that the power and information are transferred simultaneously. Fig. 16(b) similarly shows the ac currents in upward communication.

To display the details of the power waveform, the voltage and current waveforms after the inverter and before the rectifier are shown in Fig. 17. The voltage and current waveforms are depicted in Figs. 17(a1) and (b1), where the mixed power

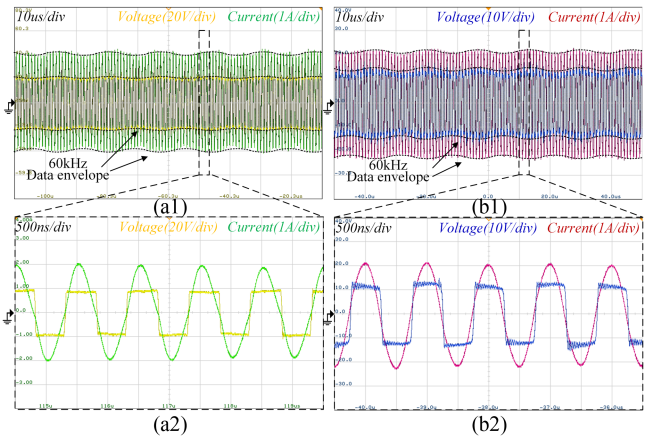

Fig. 17. Waveforms of the transmitter and receiver with downward communication. (a1) Mixed power signals after the inverter. (a2) Enlarged. (b1) Mixed power signals before the rectifier. (b2) Enlarged.

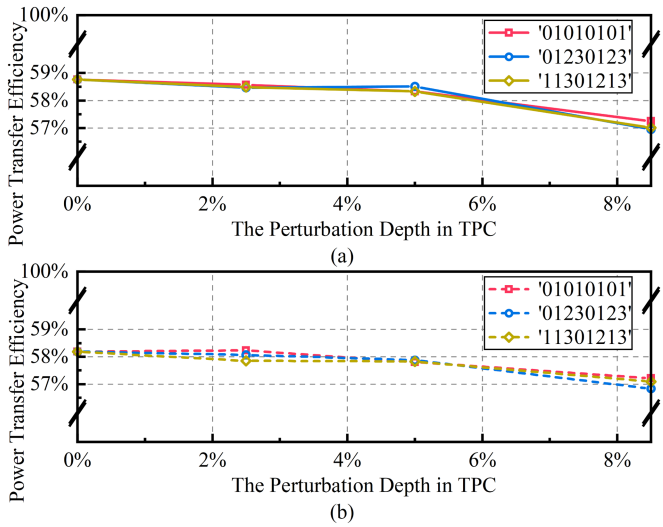

Fig. 18. Overall power transfer efficiency versus the perturbation depth in TPC. (a) Downward transmission. (b) Upward transmission.

signals are accompanied with the 60 kHz data envelope. The data envelope is similar to the principles expressed in Fig. 2. In Figs. 17(a2) and (b2), the waveforms are enlarged. The resonant state during operating is presented.

With the design of TPCs in Section IV, the influence of the small duty-cycle perturbation is studied. Defining the small perturbation over the original duty-cycle as the perturbation depth. In Fig. 18, the overall power transfer efficiency versus the perturbation depth of TPCs is depicted. The efficiency in downward communication is shown by dots with solid lines, while the efficiency in upward communication is shown by dots with dashed lines. There is no difference in the efficiency decrease caused by different data sequences. As the perturbation depth increases, the power transfer efficiency decreases. As shown in Fig. 18, when the perturbation depth is relatively small (<10%), power transmission efficiency remains nearly unaffected, and the converter maintains stable operation. The

TABLE III
COMPARISON OF MULTICOIL SWPIT TECHNIQUES

Reference	YANG ET AL. [23]	LI ET AL. [24]	This article
Power frequency	Switching between 216.6 and 303.1 kHz	200 kHz	1 MHz
Data carrier frequency	Switching between 216.6 and 303.1 kHz	1 MHz	60 kHz
Coil configuration	A series connection of a parallel *LC* branch and a series *LC* branch	Series-compensation for complete bipolar coil, and Series-compensation for two single polar coil parts	A series LC branch
Scalability in multi-coil systems	Coil reconfiguration of every coil	Coil reconfiguration of every coil	Adjust two matching resistors
Power	15 W	23.6 W	27.7 W
Efficiency	75%	70%	58%
Data rate	2 kbps	50 kbps	20 kbps

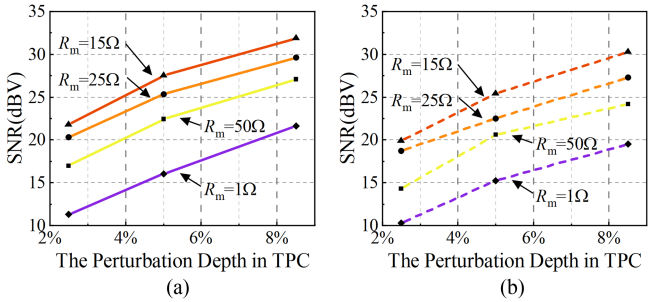

Fig. 19. SNR versus the perturbation depth. (a) Downward communication. (b) Upward communication.

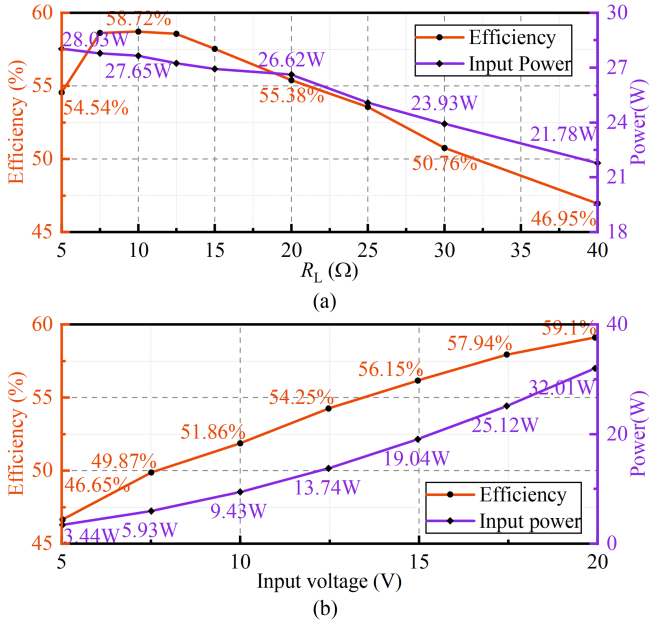

Fig. 20. System efficiency and input power versus (a) different R_L and (b) different input voltage V_{dc}.

efficiency is measured by a power analyzer (HIOKI PW8001). The overall system transfer efficiency is maintained around 58%.

The noise in the system prototype is measured, and the SNR is subsequently evaluated and presented in Fig. 19. Fig. 19(a) and (b) illustrates SNR variations with increasing perturbation depth in the downward and upward communication links, respectively. The results show that higher perturbation depths in the TPC increase the data signal amplitude, thereby improving SNR. Additionally, we evaluated the impact of matching resistors, indicated by different colored curves in Fig. 19. Optimized matching resistors enhance the data signal transmission characteristics in the MCR channel, leading to stronger received signal amplitudes and improved SNR for comparable perturbation depths.

The overall performance of the system is depicted in Fig. 20. As illustrated in Fig. 20(a), the input power and efficiency were measured under a fixed input voltage of $V_{dc} = 18.4$ V, with varying load resistance R_L. As the load increases, the system efficiency first rises and then decreases. The input power varies with the increase of the load, which is caused by the characteristics of the S-S compensation network. Fig. 20(b) shows the measurement results obtained under a fixed load R_L, with varying input voltage. As the input power increases, the system efficiency improves. However, the rate of improvement gradually slows. This trend is attributed to losses caused by switching operations. At low input power levels, the conduction losses of the switches account for a significant proportion, resulting in reduced efficiency.

Finally, the features of the proposed WPIDT system are compared with those of recently reported five-coil SWPIT systems in Table III. Yang et al. [22] and Li et al. [23] utilized novel coil configurations to optimize the multiplexed power and data transfer channel. When the number of coils changes, each coil needs to be reconfigured for compensation based on overall transfer characteristics to achieve optimal performance. For highly flexible multicoil systems, this design process can be quite complex. In contrast, the proposed WPIDT system eliminates the need for additional configuration of wireless coils. Its transfer features can be easily evaluated using *S*-parameters, a method widely adopted in practice. Due to the simple coil structure, the WPIDT system offers flexible scalability with any number of coils. Furthermore, WPIDT is well-suited for high-frequency WPT systems, which are rarely addressed in prior SWPIT research.

VI. CONCLUSION

In this article, the transfer properties of the multicoil MCR channel are derived and presented using scattering parameters. Additionally, the principle of the WPIDT system is explored,

and the analysis of the matching resistor for communication is provided. The results show that the transfer properties of duplex communication links can be optimized simultaneously, and WPIDT can be applied to MCR-WPT systems with any number of coils. Experiments show that reliable communication at a rate of 20 kbps is achieved in a 27.7 W prototype. Furthermore, since the proposed method treats the coils, front-side inverter, and load-side converter as part of the communication channel, it has the potential for application in other high-frequency WPT systems, such as capacitive power transfer systems.

REFERENCES

[1] J. Garnica, R. A. Chinga, and J. Lin, "Wireless power transmission: From far field to near field," *Proc. IEEE*, vol. 101, no. 6, pp. 1321–1331, Jun. 2013, doi: 10.1109/JPROC.2013.2251411.

[2] E. Moisello, A. Liotta, P. Malcovati, and E. Bonizzoni, "Recent trends and challenges in near-field wireless power transfer systems," *IEEE Open J. Solid-State Circuits Soc.*, vol. 3, pp. 197–213, 2023, doi: 10.1109/OJSSCS.2023.3313575.

[3] P. Wang, Y. Sun, Y. Feng, T. Feng, Y. Fan, and X. Li, "An improvement of SNR for simultaneously wireless power and data transfer system with full-duplex communication mode," *IEEE Trans. Power Electron.*, vol. 37, no. 2, pp. 2413–2424, Feb. 2022, doi: 10.1109/TPEL.2021.3106903.

[4] Y. Fan, Y. Sun, P. Deng, H. Hu, C. Jiang, and Y. Feng, "A simultaneous wireless power and high-rate data transfer system based on transient responses regulation," *IEEE Trans. Power Electron.*, vol. 38, no. 8, pp. 9362–9366, Aug. 2023, doi: 10.1109/TPEL.2023.3278749.

[5] J. Feng, G. Wei, J. Cui, J. Zhang, F. Chen, and C. Zhu, "A high-misalignment-tolerant and extensive vertical adaptation combined simultaneous transmission of power and data for WPT system," *IEEE J. Emerg. Sel. Top. Power Electron.*, vol. 11, no. 6, pp. 6138–6149, Dec. 2023, doi: 10.1109/JESTPE.2023.3323021.

[6] T. Li, Z. Sun, Y. Wang, J. Mai, and D. Xu, "Simultaneous wireless power and data transfer system with full-duplex MIMO communication channels for underwater applications," *IEEE Trans. Ind. Inform.*, vol. 20, no. 4, pp. 6382–6393, Apr. 2024, doi: 10.1109/TII.2023.3345459.

[7] Y. Yao, P. Sun, X. Liu, Y. Wang, and D. Xu, "Simultaneous wireless power and data transfer: A comprehensive review," *IEEE Trans. Power Electron.*, vol. 37, no. 3, pp. 3650–3667, Mar. 2022, doi: 10.1109/TPEL.2021.3117854.

[8] D. Ahn and S. Hong, "A study on magnetic field repeater in wireless power transfer," *IEEE Trans. Ind. Electron.*, vol. 60, no. 1, pp. 360–371, Jan. 2013, doi: 10.1109/TIE.2012.2188254.

[9] Y. Liu, Y. Li, X. Zhang, and Z. He, "Load-independent voltage-gain design method for Domino-resonator Wireless power Transfer systems," *IEEE Trans. Power Electron.*, vol. 39, no. 2, pp. 1997–2003, Feb. 2024, doi: 10.1109/TPEL.2023.3335487.

[10] A. Kurs, A. Karalis, R. Moffatt, J. D. Joannopoulos, P. Fisher, and M. Soljacic, "Wireless power transfer via strongly coupled magnetic resonances," *Science*, vol. 317, no. 5834, pp. 83–86, 2007, doi: 10.1126/science.1143254.

[11] M. Schormans, D. Jiang, V. Valente, and A. Demosthenous, "Short-range quality-factor modulation (SQuirM) for low power high speed inductive data transfer," *IEEE Trans. Circuits Syst. I-Reg. Papers*, vol. 66, no. 9, pp. 3254–3265, Sep. 2019, doi: 10.1109/TCSI.2019.2922124.

[12] X. Li, J. Hu, Y. Li, H. Wang, M. Liu, and P. Deng, "A decoupled power and data-parallel transmission method with four-quadrant misalignment tolerance for wireless power transfer systems," *IEEE Trans. Power Electron.*, vol. 34, no. 12, pp. 11531–11535, Dec. 2019, doi: 10.1109/TPEL.2019.2920441.

[13] X. Li, Z. Li, U. K. Madawala, H. Wang, Y. Sun, and X. Dai, "A simultaneous wireless power and data transfer method utilizing a novel coupler design for rotary steerable systems," *IEEE Trans. Power Electron.*, vol. 39, no. 9, pp. 11824–11833, Sep. 2024, doi: 10.1109/TPEL.2024.3409358.

[14] Y. Zhou, X. Zhu, L. Wu, and B. Wang, "Study of wireless power and information transmission technology based on the triangular current waveform," *IEEE Trans. Power Electron.*, vol. 33, no. 2, pp. 1368–1377, Feb. 2018, doi: 10.1109/TPEL.2017.2678503.

[15] J. Wu, C. Zhao, Z. Lin, J. Du, Y. Hu, and X. He, "Wireless power and data transfer via a common inductive link using frequency division multiplexing," *IEEE Trans. Ind. Electron.*, vol. 62, no. 12, pp. 7810–7820, Dec. 2015, doi: 10.1109/TIE.2015.2453934.

[16] Z. Qian, R. Yan, J. Wu, and X. He, "Full-duplex high-speed simultaneous communication technology for wireless EV charging," *IEEE Trans. Power Electron.*, vol. 34, no. 10, pp. 9369–9373, Oct. 2019, doi: 10.1109/TPEL.2019.2909303.

[17] Y. Sun, P. Yan, Z. Wang, and Y. Luan, "The parallel transmission of power and data with the shared channel for an inductive power transfer system," *IEEE Trans. Power Electron.*, vol. 31, no. 8, pp. 5495–5502, Aug. 2016, doi: 10.1109/TPEL.2015.2497739.

[18] G. Wei, J. Feng, J. Zhang, C. Wang, C. Zhu, and S. Yurievich Ostanin, "An efficient power and data synchronous transfer method for wireless power transfer system using double-D coupling coil," *IEEE Trans. Ind. Electron.*, vol. 68, no. 11, pp. 10643–10653, Nov. 2021, doi: 10.1109/TIE.2020.3038081.

[19] Y. Wang, T. Li, M. Zeng, J. Mai, P. Gu, and D. Xu, "An underwater simultaneous wireless power and data transfer system for AUV with high-rate full-duplex communication," *IEEE Trans. Power Electron.*, vol. 38, no. 1, pp. 619–633, Jan. 2023, doi: 10.1109/TPEL.2022.3203038.

[20] M. M. Ahmadi, S. Pezeshkpour, and Z. Kabirkhoo, "A high-efficiency ASK-modulated class-E power and data transmitter for medical implants," *IEEE Trans. Power Electron.*, vol. 37, no. 1, pp. 1090–1101, Jan. 2022, doi: 10.1109/TPEL.2021.3092829.

[21] C. Xia, H. Zhang, N. Wei, S. Zhao, J. Yan, and X. Song, "Simultaneous wireless power and multibit signals transfer system with hybrid modulation waves PWM control," *IEEE Trans. Power Electron.*, vol. 37, no. 10, pp. 12913–12928, Oct. 2022, doi: 10.1109/TPEL.2022.3178998.

[22] X. Yang, Y. Li, W. Sun, J. Chen, Y. Peng, and Z. He, "A simultaneous power and data transfer technology using dual-resonance-band circuits for Domino-resonator WPT systems," *IEEE Trans. Ind. Inform.*, vol. 20, no. 1, pp. 269–279, Jan. 2024, doi: 10.1109/TII.2023.3261887.

[23] Y. Li, X. Yang, W. Sun, J. Hu, and Z. He, "A simultaneous power and data transmission technology based on coil multiplexing in Domino-resonator WPT systems," *IEEE Trans. Power Electron.*, vol. 38, no. 3, pp. 2878–2883, Mar. 2023, doi: 10.1109/TPEL.2022.3225479.

[24] X. He et al., "Wireless power and information dual transfer system via magnetically coupled resonators," *Commun. Eng.*, vol. 3, no. 1, 2024, Art. no. 8, doi: 10.1038/s44172-023-00154-4.

[25] Z. Dong, S. Liu, X. Li, Z. Xu, and L. Yang, "A novel long-distance wireless power transfer system with constant current output based on domino-resonator," *IEEE J. Emerg. Sel. Top. Power Electron.*, vol. 9, no. 2, pp. 2343–2355, Apr. 2021, doi: 10.1109/JESTPE.2020.2983231.

[26] A. P. Sample, D. A. Meyer, and J. R. Smith, "Analysis, experimental results, and range adaptation of magnetically coupled resonators for wireless power transfer," *IEEE Trans. Ind. Electron.*, vol. 58, no. 2, pp. 544–554, Feb. 2011, doi: 10.1109/TIE.2010.2046002.

[27] X. He, R. Wang, J. Wu, and W. Li, "Nature of power electronics and integration of power conversion with communication for talkative power," *Nat. Commun.*, vol. 11, no. 1, 2020, Art. no. 2479, doi: 10.1038/s41467-020-16262-0.

Wanying Weng (Student Member, IEEE) received the B.Sc. degree in electrical engineering from Zhejiang University, Hangzhou, China, in 2020. She is currently working toward the Ph.D. degree in power electronics with the College of Electrical Engineering, Zhejiang University, Hangzhou, China.

Her current research interests include MHz wireless power transfer and communication technique in wireless power system.

Jiande Wu (Senior Member, IEEE) was born in Zhejiang, China, in 1973. He received the B.Sc., M.Sc., and Ph.D. degrees in power electronics from the College of Electrical Engineering, Zhejiang University, Hangzhou, China, in 1994, 1997, and 2012, respectively.

Since 1997, he has been a Faculty Member with Zhejiang University, where he is currently an Associate Professor. From 2013 to 2014, he was an Academic Visitor with the University of Strathclyde, Glasgow, U.K. His research interests include power electronics control, distributed power electronics system and fieldbus communication.

Long Qin received the B.Sc. degree in power electronics in 2022 from the College of Electrical Engineering, Zhejiang University, Hangzhou, China, where he is currently working toward M.Sc. degree in power electronics with the College of Electrical Engineering.

During his study, he focuses on simultaneous wireless power and information transfer technology.

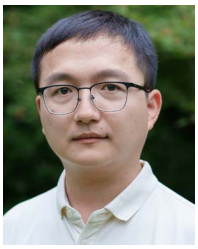

Hao Chen received the B.Sc. and M.Sc. degrees in power electronics and electrical engineering in 2019 and 2022, respectively, from Zhejiang University, Hangzhou, China, where he is currently working toward the Ph.D. degree in power electronics. From 2022 to 2024, he was a Research Assistant with the University of British Columbia, Vancouver, BC, Canada. His research interests include communication techniques applied in power electronics and wireless power transfer.

Yan Deng (Senior Member, IEEE) received the B.E.E. degree in electrical engineering in 1994 from the Department of Electrical Engineering, and the Ph.D. degree in power electronics and electric drives from the College of Electrical Engineering, Zhejiang University, in 1994 and 2000, respectively.

He is currently a Full Professor with the College of Electrical Engineering, Zhejiang University, and the Head of the Research Group for Energy Network Transition, Hangzhou, China. He has authored or coauthored 130 publications, many in IEEE journals, and holds more than 20 patents. His research interests include power electronics, renewable energy, and power supply systems.

Dr. Deng is an active and significant contributor to the IEEE community.

Xiangning He (Fellow, IEEE) received the B.Sc. and M.Sc. degrees in power electronics from Nanjing University of Aeronautical and Astronautical, Nanjing, China, in 1982 and 1985, respectively, and the Ph.D. degree in power electronics from Zhejiang University, Hangzhou, China, in 1989.

In 1991, he was a Fellowship from the Royal Society of U.K., and conducted research in Heriot-Watt University, Edinburgh, U.K., as a Post-Doctoral Research Fellow for two years. In 1994, he was an Associate Professor with Zhejiang University. Since 1996, he has been a Full Professor with the College of Electrical Engineering, Zhejiang University. His research interests are power electronics and their industrial applications.